A new incompressible Navier-Stokes solver combining Fourier pseudo-spectral and immersed boundary methods

F.P. Mariano[1], **L.Q. Moreira**[1], **A. Silveira-Neto**[1]
C.B. da Silva [2] **and J.C.F. Pereira**[2]

Abstract: A new numerical methodology combining Fourier pseudo-spectral and immersed boundary methods - *IMERSPEC* - is developed for fluid flow problems governed by the incompressible Navier-Stokes equations. The numerical algorithm consists in a classical Fourier pseudo-spectral methodology using the collocation method where wall boundary conditions are modelled by using an immersed boundary method (IBM). The performance of that new methodology is exemplified in two-dimensional numerical simulations of Green-Taylor decaying vortex, lid-driven cavity and flow over a square cylinder. The convergence rate, the accuracy, the influence of the Reynolds number and the external domain size are analyzed. This new method combines some advantages of high accuracy and low computational cost provided by Fourier pseudo-spectral methods (FPSM) with the possibility of tackling complex geometries given by immersed boundary method.

Keywords: Numerical Simulations; Navier-Stokes; Fourier Pseudo-spectral; Immersed Boundary.

1   Introduction

The last two decades a lot of effort has been spent by the fluid dynamic scientific community to address two crucial but conflicting key issues in the science of computational fluid dynamics (CFD). These are associated with a needind to model increasingly complex boundary conditions in one hand, and requiring high accuracy on the other [Ferziger and Peric (1996)].

The great majority of engineering and geophysical fluid flow problems are characterized by highly complex geometries that arising mainly from the geometry of boundary conditions, which are often associated with the presence of solid, moving

---

[1] Laboratory Mechanical of Fluids - MFlab, Faculty of Mechanical Engineering - FEMEC, Federal University of Uberlândia - UFU, Uberlândia-MG, Brasil.
[2] Instituto Superior Técnico, LASEF, Lisboa, Portugal.

or flexible walls. The flow inside combustion chambers, around moving vehicles, inside deformable, or elastic, biological bodies are just a few common examples of fluid flow problems where geometrical complex wall boundaries normally complicate the numerical algorithm.

In order to be able to cope with complex boundary conditions, whole families of numerical techniques and methods have been developed. A method widely used consists in representing the geometry with body-fitted coordinates. Curvilinear grids [Marchioli, Armenio, and Soldati (2007)], non-orthogonal grids [Xu and Zhang (1999); Sousa (2005)], and non-structured grids [Mavriplis (1997); Barton, Markham-Smith, and Bressloff (2002)] that represent three different approaches within this strategy.

However, increasing topological and geometrical complexity of the computational grids tend to be associated with a decreasing of the overall accuracy of numerical methods. For instance, most non-structured Navier-Stokes solvers display less than two order of accuracy. Indeed, to produce a non-structured fluid flow code with second order accuracy remains a formidable challenge [Kobayashi, Pereira, and Pereira (1999)]. Another greater problem related to these approaches is their extremely high computational cost, both in terms of CPU time and memory storage. This fact alone, probably, stands for the reason preventing a wider use of large-eddy simulations (LES) of turbulent flows in complex geometries which are usually associated with engineering applications.

The quest for high order accuracy has also been the subject of some numerical development [Lele (1992); Karniadakis and Sherwin (1999)]. A highly accurate Navier-Stokes solver allows to obtain a better solution of a given flow problem in a given grid, or a smaller grid size, than as compared with a less accurate code.

In terms of high order accuracy, the family of the so called spectral methods [Canuto, Hussaini, Quarteroni, and Zang (1987)] has been virtually unsurpassed. Spectral methods are characterized by exponential convergence to the exact solution with increasing grid size. Within the family of spectral methods, the classical pseudo-spectral collocation method is probably the most impressive due to its extremely high accuracy and its low computational cost in terms of memory storage. Moreover, since the pressure terms in the Navier-Stokes equations can be lumped together with the non-linear term (see section 2), the pseudo-spectral collocation method does not require the solution of a Poisson equation for the pressure field, which results in an unusually fast time stepping procedure. These classical methods, however, are in general not applicable to complex flow geometries. The collocation method in particular, can be only used in flows with periodic boundary conditions directions, which excludes its use in most general engineering configurations.

Recently, new numerical methodologies have appeared allowing the inclusion of geometrically complex boundary conditions without increasing considerably the computational cost and complexity of the computational grids, namely, virtual and immersed boundary methods [Peskin (1972, 1977); Unverdi and Tryggvason (1992); Goldstein, Adachi, and Sakata (1993); Mittal and Iaccarino (2005); Choi, Oberoi, Edwards, and Rosati (2007)] which make possible by adding a source term to the Navier-Stokes equations, to include relatively complex shapes of wall boundaries in what are essentially algorithms designed for Cartesian meshes.

These methods have been used successfully in a variety of flow configurations within finite-difference [Silva, Silveira-Neto, and Damasceno (2003)] and finite-volume methods [Johansen and Collela (1998); Silvestrini and Lamballais (2002)], to more complex applications involving the simulation of the flow field past a pick-up truck [Kalitzin and Iccarino (2003)]. These methods have produced good results with smaller computational costs than other more conventional methods using non-orthogonal or non-structured grids (see [Iaccarino and Verzicco (2003); Kim, Kim, and Choi (2001)]). Despite the continuous improvement in the immersed boundary methods, the main drawback of these methods are their relatively small accuracy near the walls, which is caused by the relatively small number of grid points used to define them (*e.g.* see [Silva, Silveira-Neto, and Damasceno (2003); Lai and Peskin (2000); Peskin (2002)]).

The goal of the present work is to develop a new method for simulating incompressible flows with wall boundary conditions, which combines the accuracy and low computational cost of the classical Fourier pseudo-spectral method with flexibility in handling complex geometries allowed by the immersed boundary methods. We introduce, specifically, the *IMERSPEC* method, which combines a classical pseudo-spectral (collocation) method [Canuto, Hussaini, Quarteroni, and Zang (1987)], where any spatial derivative is computed with spectral accuracy, with an immersed boundary method, which, in order to model the effects arising from the presence of complex shape wall boundaries we use the technique proposed by [Silva, Silveira-Neto, and Damasceno (2003)] named Virtual Physical Model - VPM.

The first tests of *IMERSPEC* methodology, simulations of classical CFD problems are carried out with cartesian geometries and coincidence between Eulerian collocation points and Lagrangian interface (for more details see section 2). Despite flow simulations over simple geometry this strategy allowed to validate the methodology. Furthermore, several problems can be solved with cartesian geometries, for example, free shear flows (jets, mixing layers), flat plate boundary layer and imposition of boundary conditions. In this paper, simulations of lid driven cavity flow and flow over square cylinder are performed. It is interesting to observe the compu-

tational efficiency of Fourier pseudo-spectral method even it requires extra buffer domain.

The present paper is organized as follows. Sec. 2 focuses on the philosophy of the present methodology and describes the mathematical formulation of the pseudo-spectral and immersed boundary methods. Sec. 3 describes the numerical methods and computational details of the presented simulations. The results are discussed in Sec. 4, first beginning with a verification of the pseudo-spectral schemes in the Taylor-Green flow [Taylor and Green (1937)] and before presenting the results obtained in the lid-driven cavity [Ghia, Ghia, and Shin (1982)]. For this flow configuration, the effects of resolution, Reynolds number, and external domain size are analyzed in detail through comparisons obtained from the literature [Ghia, Ghia, and Shin (1982); Hou, Zou, Chen, Doolen, and Cogley (1995); Botella and Peyret (1998); Erturk, Corke, and Göcçöl (2005)]. In addition, the *IMERSPEC* methodology is also applied to the flow over a square cylinder [Sohankar (2006); Chen, Chang, and Sun (2007)]. Finally, in Sec. 5, an overview of the main results and conclusions are presented.

2   Mathematical formulation

The main idea of the present methodology consists in merging the immersed boundary concept into a classical Fourier pseudo-spectral method. We start writing the governing equations in physical and in Fourier space. Then, follows the description of the pseudo-spectral and immersed boundary methods. Finally, the philosophy of the coupling of both methods is described.

2.1   Governing Equations

This work is restricted to Newtonian fluids and incompressible flows, which are governed by Navier-Stokes and continuity equations. In the physical space and for an inertial reference frame these equations are:

$$\frac{\partial u_i}{\partial t} + \frac{\partial (u_i u_j)}{\partial x_j} = -\frac{1}{\rho}\frac{\partial p}{\partial x_i} + \nu\frac{\partial^2 u_i}{\partial x_j \partial x_j} + f_i, \tag{1}$$

$$\frac{\partial u_i}{\partial x_i} = 0, \tag{2}$$

where $u_i(\vec{x},t)$ and $p(\vec{x},t)$ are the velocity and pressure fields, respectively; ρ is the fluid density and ν is the fluid kinematic viscosity. The term $f_i(\vec{x},t)$ represents a given source term.

Defining the two-dimensional (2D) direct Fourier transforms of the velocity and pressure fields,

$$\widehat{u}_i(\vec{k},t) = \left(\frac{1}{2\pi}\right)^2 \int_{-\infty}^{+\infty} u_i(\vec{x},t)e^{-\iota\vec{k}.\vec{x}}d\vec{x}, \tag{3}$$

$$\widehat{p}(\vec{k},t) = \left(\frac{1}{2\pi}\right)^2 \int_{-\infty}^{+\infty} p(\vec{x},t)e^{-\iota\vec{k}.\vec{x}}d\vec{x}, \tag{4}$$

and the inverse (2D) Fourier transforms,

$$u_i(\vec{x},t) = \int_{-\infty}^{+\infty} \widehat{u}_i(\vec{k},t)e^{\iota\vec{k}.\vec{x}}d\vec{k}, \tag{5}$$

$$p(\vec{x},t) = \int_{-\infty}^{+\infty} \widehat{p}(\vec{k},t)e^{\iota\vec{k}.\vec{x}}d\vec{k}. \tag{6}$$

And applying direct Fourier transforms to Eqs. (1) and (2) the Navier-Stokes and continuity equations can be obtained in the Fourier space [Mariano (2007)]:

$$\left(\frac{\partial}{\partial t} + \nu k^2\right)\widehat{u}_i(\vec{k},t) = -\iota k_i\widehat{p}(\vec{k},t) + \iota k_j \int_{\vec{k}=\vec{r}+\vec{s}} \widehat{u}_i(\vec{r},t)\widehat{u}_j(\vec{k}-\vec{r},t)d\vec{r}$$
$$+\widehat{f}_i(\vec{k},t), \tag{7}$$

$$\iota k_i\widehat{u}_i(\vec{k},t) = 0, \tag{8}$$

where $\vec{k}$, $\vec{r}$ and $\vec{s}$ are wave number vectors, $k = |\vec{k}|$ is the wave number norm and ι is the imaginary unit. In Eq. (7) the two terms on the left-hand side represent the local acceleration and viscous terms, while the three terms on the right-hand side represent the pressure, the non-linear and the forcing terms, respectively.

Fig. 1 illustrates the geometrical relationships among all terms from Eq. (7) in the Fourier space. Defining a Π plane to which the wave number vector $\vec{k}$ is perpendicular. Eq. (8) shows that the incompressibility condition implies that any given Fourier coefficient $\widehat{u}_i(\vec{k},t)$ is perpendicular to the local wave number $\vec{k}$ and thus it belongs to this plane.

Consequently, we can see that the left hand side of Eq. (7) is also in Π plane. Therefore, the sum of the whole right-hand side of this equation consisting in the sum of the pressure, the non-linear and the forcing terms that there is also in Π plane. Moreover, since the pressure term is perpendicular to Π plane this sum will be also equal to the sum of the non-linear and forcing terms projected into Π plane. It follows that the Navier-Stokes equations in the Fourier space can be re-written as:
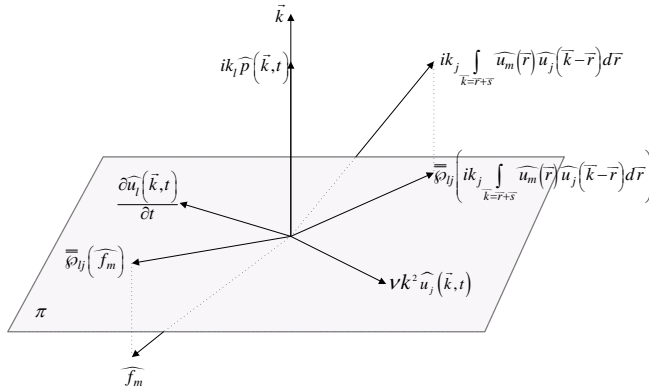
Figure 1: Representation of terms from Eq. 7 in Fourier space and their relation to the plane Π, defined as being orthogonal to the wave number vector.

$$\left(\frac{\partial}{\partial t} + \nu k^2\right)\widehat{u}_i(\vec{k},t) = P_{il}\left(\imath k_j \int_{\vec{k}=\vec{r}+\vec{s}} \widehat{u}_l(\vec{r},t)\widehat{u}_j(\vec{k}-\vec{r},t)d\vec{r} + \widehat{f}_l(\vec{k},t)\right),\tag{9}$$

where $P_{il}(\vec{k})$ is the projection operator defined by

$$P_{il}(\vec{k}) = \delta_{il} - \frac{k_i k_l}{k^2},\tag{10}$$

which projects any given vector into Π plane (δ_{ij} is the Kronecker tensor). An equation for the pressure field can be obtained by multiplying both sides of Eq. (7) by $\imath k_i$, giving,

$$\widehat{p}(\vec{k},t) = \frac{k_i k_j}{k^2}\int_{\vec{k}=\vec{r}+\vec{s}} \widehat{u}_i(\vec{r},t)\widehat{u}_j(\vec{k}-\vec{r},t)d\vec{r} - \frac{\imath k_i \widehat{f}_i(\vec{k},t)}{k^2}.\tag{11}$$

It should be useful to stress that Eq. 11 is used only if the calculation of the pressure field is aimed.

2.2 Fourier pseudo-spectral method

The main idea of the pseudo-spectral method consists in not evaluating directly the convolution integral defining the non-linear terms in Eq. (9). The spatial velocity derivatives involved in the non-linear term are computed in the Fourier space according to

$$\frac{\partial (u_i u_j)}{\partial x_j}(\vec{x},t) = \int_{-\infty}^{+\infty} -\imath k_j \widehat{u_i u_j}(\vec{k},t)e^{\imath \vec{k}.\vec{x}}d\vec{k}\tag{12}$$

while all the products are performed in the physical space, by make using of the inverse Fourier transform defined by Eq. (5). In the present work we used the equivalent skew-symmetric formulation of the non-linear terms proposed by [Canuto, Hussaini, Quarteroni, and Zang (1987)].

2.3 Immersed boundary method

The immersed boundary method used in this work is based on the method described in [Silva, Silveira-Neto, and Damasceno (2003)]. It uses the concept of Eulerian and Lagrangian domains (in the physical space). The two domains are exemplified in Fig. 2, where $\vec{x}$ represents a given point in the Eulerian domain Ω while $\vec{x}_k$ represents a point in the Lagrangian surface Γ. The Eulerian domain Ω consists
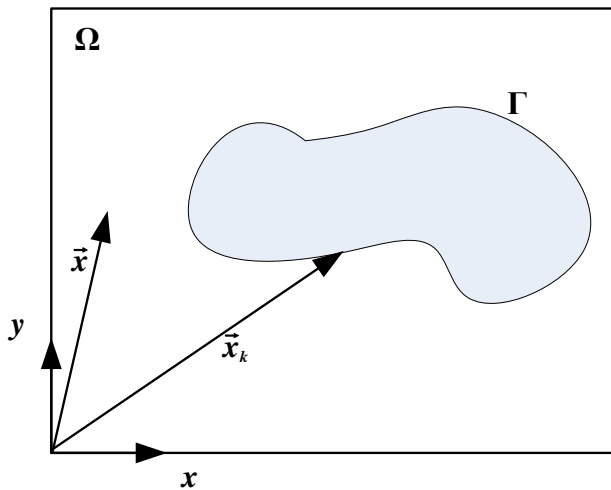

Figure 2: Sketch of Eulerian and Lagrangian domains.

in the whole region of space containing the fluid flow problem at study, including the region in the interior of any given solid body immersed in the flow. Within this domain we define the Lagrangian domain Γ as the line or surface representing the wall boundaries.

As explained in [Silva, Silveira-Neto, and Damasceno (2003)], the immersed boundary method allows the specification of a particular boundary condition in the flow through the addition of a source term $f_i(\vec{x}, t)$ to the Navier-Stokes equations. This

source term $f_i(\vec{x},t)$ is defined by

$$f_i(\vec{x},t) = \begin{cases} F_i(\vec{x}_k,t) & \text{if } \vec{x} = \vec{x}_k \\ 0 & \text{if } \vec{x} \neq \vec{x}_k \end{cases} \tag{13}$$

where $F_i(\vec{x}_k,t)$ is modelled by applying the second law of the Newtonian dynamics to a fluid particle located at the interface, Γ.

Considering a fluid particle placed at the Lagrangian point $\vec{x}_k$ and at a time t, a balance of linear momentum applied to this fluid particle yields the following equation for the resulting force acting upon it,

$$F_i(\vec{x}_k,t) = \rho \frac{\partial u_i}{\partial t}(\vec{x}_k,t) + \rho \frac{\partial(u_i u_j)}{\partial x_j}(\vec{x}_k,t) + \frac{\partial p}{\partial x_i}(\vec{x}_k,t) - \mu \frac{\partial^2 u_i}{\partial x_j \partial x_j}(\vec{x}_k,t). \tag{14}$$

We can see that the computation of $F_i(\vec{x}_k,t)$ requires spatial and temporal derivatives of velocity and pressure fields at the interface $\vec{x}_k$. $F_i(\vec{x}_k,t)$ is defined only over the fluid-solid interface, *i.e.* over the Lagrangian surface Γ. The computation of the temporal and the spatial derivative appeared in Eq. (14) is detailed next section.

2.4   *Merging the pseudo-spectral and immersed boundary methods*

The originality of the present work lies in one key idea: the use of Fourier pseudo-spectral methods to simulate non-periodic problems. This is achieved by the *IMERSPEC* methodology proposed in this work, allowing the merged of the pseudo-spectral and the immersed boundary methods.

With the *IMERSPEC* methodology we define two domains as illustrated in Fig. 3 for the general case of a flow around several complex shaped bodies. The region of space under study defines the interior domain Ω_I, while outside this region it is defined a buffer domain Ω_B. The whole Eulerian domain consists, then, in the union between the interior and the buffer domains $\Omega = \Omega_I \bigcup \Omega_B$. We denote by Γ_{BC} the Lagrangian surface representing the surface surrounding Ω_I, and by Γ_i the Lagrangian surface representing the surface surrounding the body i ($i = 1, ..., N_b$), where N_b is the number of bodies inside Ω_I. Then the full Lagrangian set is the union of Γ_{BC} with all Γ_i *i.e.* $\Gamma = \Gamma_{BC} \bigcup_{i=1}^{N_b} \Gamma_i$. The immersed boundary method is applied on Γ_{BC}, in order to prescribe the boundary conditions surrounding the domain of the flow at study in Ω_I, and also in each Γ_i, in order to describe any given complex shaped bodies within Ω_I. Notice that the buffer domain Ω_B serves as a region of space where the flow is given room to adjust "naturally" from the periodic boundary conditions imposed at its external limits, and to the boundary conditions prescribed by the immersed method at Γ_{BC}.

In order to close the coupling between the pseudo-spectral and the immersed boundary methods the term $f_i(\vec{x}_k, t)$ in Eq. (1) has to be evaluated. This requires the computation of several spatial and temporal derivatives at each point $\vec{x}_k$ and time t in the definition of $F_i(\vec{x}_k, t)$ given by Eq. (14). To achieve this we define the following velocity fields, considering an inertial reference frame, $u_i(\vec{x}, t)$ as the fluid velocity at the Eulerian point $\vec{x}$, where $\vec{x} \in \Omega$, and $V_i(\vec{x}_k, t)$ is the velocity of the Lagrangian surface point $\vec{x}_k$, where $\vec{x}_k \in \Gamma$.

It is important to notice that $u_i(\vec{x}, t)$ is a solution of the Navier-Stokes Eqs. (1) and (2), whereas $V_i(\vec{x}_k, t)$ is imposed by the particular flow problem at study. We also define an auxiliary velocity field $v_i^a(\vec{x}, t)$, by

$$v_i^a(\vec{x}, t) = \begin{cases} u_i(\vec{x}, t) & \text{if } \vec{x} \neq \vec{x}_k \\ V_i(\vec{x}_k, t) & \text{if } \vec{x} = \vec{x}_k. \end{cases} \tag{15}$$

With these definitions the computation of all terms involving spatial derivatives of the velocity field in Eq. (14), it can be carried out in a straightforward way, by using the auxiliary velocity field $v_i^a(\vec{x}, t)$ and the pseudo-spectral methods. The spatial derivative involving the pressure field is computed with the spectral pressure $\widehat{p}(\vec{x}, t)$ obtained through Eq. (11). Finally, the temporal derivative (first term in the right-hand side of Eq. 14) is computed using the velocity difference between $V_i(\vec{x}_k, t)$ and $u_i(\vec{x} = \vec{x}_k, t)$.
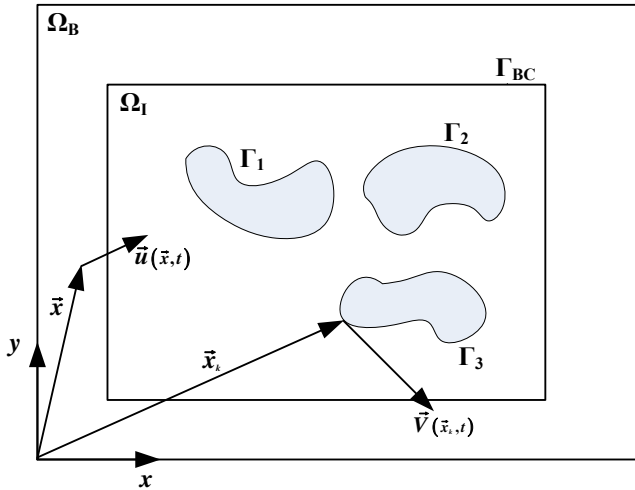

Figure 3: Sketch of Eulerian and Lagrangian domains with boundary conditions and multiples bodies.

Notice that for non-accelerated immersed boundaries *i.e.* whenever $\frac{\partial V_i(\vec{x}_k,t)}{\partial t} = 0$ this last term is zero at any point $\vec{x}_k$ where the enforced boundary condition is rigorously verified. In general, however, this term is non-zero and acts as an additional forcing term directing the immersed boundary method into a consistent physical solution.

3   Computational Details

Several aspects of numerical implementation used in all the simulations of the present paper are discussed in this section. Eq. (7) is discretized using N_x collocation points equally spaced with $\Delta x = L_x/N_x$, where L_x is the domain length in the $x - direction$ (the same procedure is adopted in the $y - direction$). In order to compute the FFTs (section 3.1) the $FFTE$ algortim, [Takahashi (2001)], is used. The Convolution integral is replaced by a pseudo-spectral method discussed in section 3.2. Other aspects like the temporal evolution and filtering are treated in sections 3.3 and 3.4, respectively.

3.1   DFT and FFT

Discret Fourier Transform (DFT) is the proper numerical way of evaluate the Eqs. (3) and (4), and its inverse form (DFTI) for Eqs. (5) and (6). DFT of a *f* function is define by [Briggs and Henson (1995)] as:

$$\widehat{f}(\vec{k}) = \sum_{n=-N/2+1}^{N/2} f_n(\vec{x}) e^{\frac{-\imath.2.\pi.\vec{k}.n}{N}} \tag{16}$$

where $\vec{k}$ is a wave number vector, N is the number of collocation points in discretized domain and n get the position of collocation points *i.e.* $x_n = n\Delta x$.

The DFT is restricted by periodics boundary conditions problems by limiting the use of numerical Fourier transform for CFD problems. Fourier spectral method is only used in simulations of temporal jets and homogeneous and isotropic turbulence.

[Cooley and Tukey (1965)] proposed the Fast Fourier Transform (FFT) algorithm, that solves the Eq. 16 very efficiently. In terms of float points operations the FFT given $O(Nlog2N)$, whereas the DFT is of order $O(N^2)$ float points operations, where N is the number of collocation points. In the present paper we used $FFTE$ subroutine, and it is implemented by [Takahashi (2001)].

3.2   Treatment of the non-linear term

The non-linear terms in Eq. (9) can be handled through different methods: advective, divergent, skew-symmetric, or rotational [Canuto, Hussaini, Quarteroni, and

Zang (1987)]. The several discretization methods present distinct properties *e.g.* the skew-symmetric form is more stable and presents the best results, but it is twice more expensive than the rotational form. However this inconvenience can be solved using the alternate skew-symmetric form. This consists in alternating the advective and divergent forms at each time step [Miksad, Akylas, and Hebert (1987)] and this is the procedure adopted in the present work. The non-linear terms require the computation of a convolution integral which is known to be computationally expensive. To overcome this problem the pseudo-spectral method is used. It consists in calculating the velocity product in the physical space and transforming this product into the spectral space.

3.3 Filtering

It is well known that when near discontinuities the Fourier spectral method may lead to spurious oscillations affecting the high wave numbers, which consist in the so called Gibbs phenomenon [Canuto, Hussaini, Quarteroni, and Zang (1987)]. In particular Gibbs oscillations can arise when we solve the Eqs. (13) and (15), which are discontinuos. In order to prevent these errors we use the following filter:

$$\widehat{f(\vec{k})}_{filtered} = \sigma(\theta)\widehat{f(\vec{k})} \tag{17}$$

where $\sigma(\theta)$ is the filter function. The sharpened raised cosine filter, proposed by [Kopriva (1986)], is used:

$$\sigma(\theta) = \sigma_0^4(35 - 84\sigma_0 + 70\sigma_0^2 - 20\sigma_0^3), \tag{18}$$

where σ_0 is given by:

$$\sigma_0 = 1/2(1 + cos\theta), \tag{19}$$

and $\theta = L\vec{k}/N$, where L is the length of domain, $\vec{k}$ is the wave number and N is the number of collocation points.

3.4 Temporal evolution

For time evolution, the low-dissipation and the low-dispersion forth-order Runge-Kutta algorithm proposed by [Berland, Bogey, and Bailly (2006)] was chosen in order to maintain the accuracy. The time step, Δt, is based in CFL criterion [Ferziger and Peric (1996)], which gives the stability of temporal advancement:

$$\Delta t = CFL.min\left[min\left[\frac{\Delta x}{max[|u|]}; \frac{\Delta y}{max[|v|]}\right]; \frac{2}{v}\left(\frac{1}{\Delta x} + \frac{1}{\Delta y}\right)^{-1}\right], \tag{20}$$

where CFL is a number between 0 and 1.

4   Results and Discussion

The main results concern with well known 2D lid-driven cavity flow - LDC [Ghia, Ghia, and Shin (1982); Hou, Zou, Chen, Doolen, and Cogley (1995); Botella and Peyret (1998); Erturk, Corke, and Göççöl (2005)], which has been used extensively in order to test, to analyse and to validate new numerical algorithms. The LDC flow for different Reynolds numbers and the influence of the inner domain size on the accuracy of the method is presented. The simulations of the flow over a square cylinder are also presented and several comparisons are carried out.

The two-dimensional pseudo-spectral algorithm used here was developed by modifying a classical three-dimensional pseudo-spectral code (using the collocation method) has already used by the authors in direct numerical simulations of isotropic turbulence and turbulent plane jets [da Silva and Pereira (2004, 2005)]. Before analysing the LDC flow it is important to demonstrate that this 2D pseudo-spectral algorithm used as a basis in the present methodology is indeed well implemented. This is the subject of the next section.

4.1   The Taylor-Green flow

The two-dimensional Taylor-Green flow consists in an array of periodic and decay counter-rotating cells, where the velocity and the pressure fields are described by simple analytical solutions to the 2D Navier-Stokes equations [Uhlmann (2005); Kim, Kim, and Choi (2001)]. The main goal is to validate the numerical implementation of the classical Fourier pseudo-spectral algorithm which is the core of the new methodology proposed in this work.

The u and v velocity components for the Taylor-Green flow are given by the following analytical expressions,

$$u_a(x,y,t) = -U\cos\left(\frac{2\pi x}{L}\right)\sin\left(\frac{2\pi y}{L}\right)e^{\frac{-2vt}{L^2}}, \tag{21}$$

$$v_a(x,y,t) = U\sin\left(\frac{2\pi x}{L}\right)\cos\left(\frac{2\pi y}{L}\right)e^{\frac{-2vt}{L^2}}, \tag{22}$$

where U is the amplitude of the velocity field and v is the kinematic viscosity. Using Eqs. (21) and (22) an analytical expression for the pressure field can be obtained by solving a Poisson equation. The result writes,

$$p_a(x,y,t) = -\frac{\rho U^2}{4}\left[\sin\left(\frac{4\pi x}{L}\right)+\cos\left(\frac{4\pi y}{L}\right)\right]e^{\frac{-4vt}{L^2}}. \tag{23}$$

4.1.1 The Taylor-Green flow without immersed boundary

The simulation domain consists in a square of sides $L_x = L_y = 2\pi \ [m]$ discretized with (16×16) collocations nodes. The Reynolds number is defined as in [Kim, Kim, and Choi (2001)]:

$$Re = \frac{UD}{\nu}, \tag{24}$$

where $D = \pi \ [m]$ is the size of a vortex, $U = 1.0 \ [m/s]$ and $Re = 10.0$. Therefore, kinematic viscosity is calculated using Eq. (24), giving $\nu = \pi/10 \ [m^2/s]$. We use $CFL = 10^{-2}$, in order to leave the error only at spatial discretization. Fig. 4 shows
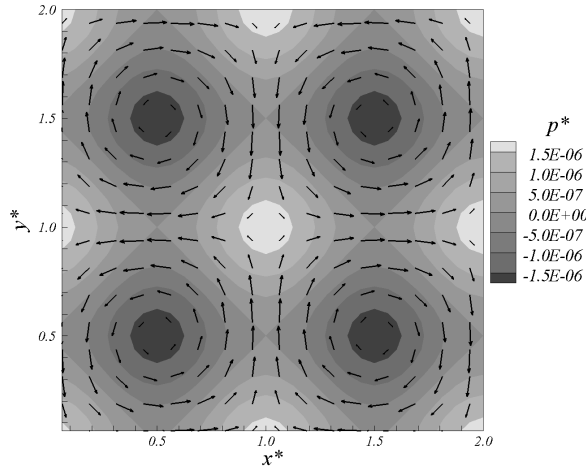
Figure 4: Pressure field superposed by velocity vectors.

contours of pressure and velocity vectors, note that the dimensions of the domain on Fig. 4 are non-dimensionalized by D. The flow exhibits of the well known Taylor-Green cells arranged in their periodic behavior, where the center of each cell corresponds to a minimum in the pressure field - Fig. 4. The number of cells along each spatial direction is imposed by the size of the computational domain. Here, we have two cells in each direction and these cells are rotating in opposite directions. In order to know the accuracy of methodology implemented the L_2 norm is evaluated:

$$L_{2\phi} = \sqrt{\frac{1}{N_x}\frac{1}{N_y}\sum_{\eta=1}^{N_x}\sum_{\mu=1}^{N_y} \parallel \phi(x_\eta, y_\mu, t) - \phi_a(x_\eta, y_\mu, t) \parallel^2}, \tag{25}$$

where ϕ is a given flow quantity, ϕ_a is the analytical solution done by Eqs. (21) - (23) N_x and N_y is the number of collocation nodes in each domain direction.

The temporal evolution for L_2 norm of the u-velocity component and pressure is shown in Fig. 5. Despite coarse mesh the errors are around zero machine (round-
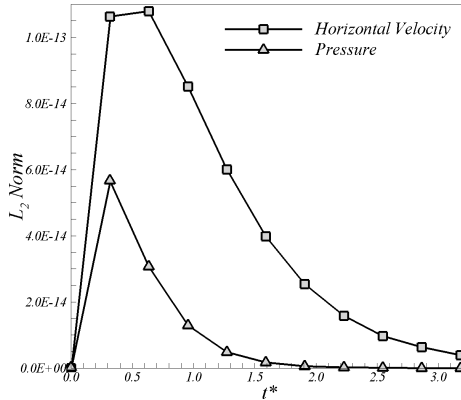

Figure 5: Temporal evolution of L_2 norm for simulations without IB.

off errors), as expected from a Fourier pseudo-spectral code. Similar results were obtained for the v-velocity. The results described above using the Taylor-Green flow show that the pseudo-spectral algorithm, used as a basis for the *IMERSPEC* method is indeed well implemented. The next subsection describes the results from the full *IMERSPEC* procedure.

4.1.2   *The Taylor-Green flow with immersed boundary*

The next example is used to assess the implementation of the IB methodology. The same idea used in [Kim, Kim, and Choi (2001)] and [Uhlmann (2005)] is used here and it consists in an embedded square geometry (Lagrangian domain Γ) inside an Eulerian domain (Ω) as shown in Fig. 6.

The Eq. (15) is available with $V_i(\vec{x}_k, t + \Delta t) = u_{ai}(\vec{x}_k, t + \Delta t)$, where u_a is defined by Eqs. (21) and (22) for each velocity components. Dimensionless mesh size ($h^* = \Delta x/D$) and different CFL numbers are simulated. L_2 norm is present for $t = 0.3\,[s]$ as shows in Fig. 7.

The results of Fig. 7 show that IB methodology using VPM provide second order convergence rate, when coupled with Fourier pseudo-spectral methodology. However accuracy order is very dependent of CFL number. This is maybe due to the temporal derivative, first term in the right-hand side of Eq. (14).
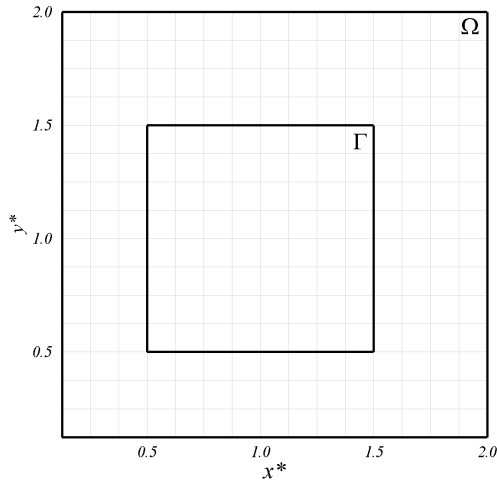
Figure 6: The Eulerian Ω and Lagrangian Γ domains used in Taylor-Green flow including an immersed boundary.

The comparison between previous simulations of the Taylor-Green flow problem with and without IB is provided in Fig. 8. It shows the absolute vorticity error
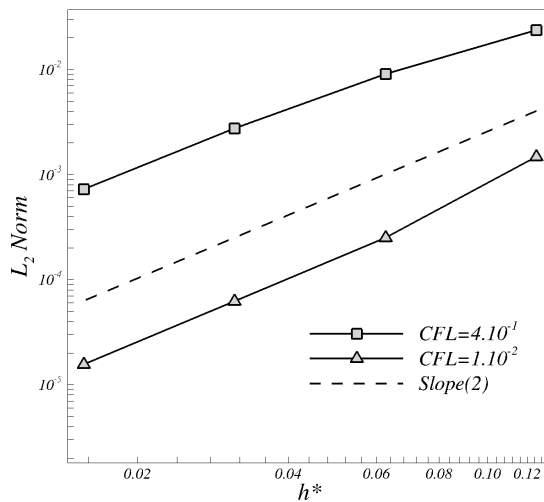

Figure 7: Order of convergence rate of L_2 norm for u-velocity component. Slope(2) is the theoretical line of second order convergence rate.

without (a) and with (b) IB. It is possible to see that the effect of force field produces the largest errors (order 10^{-4}), On the orther hand, without IB the errors is of the order 10^{-16}.
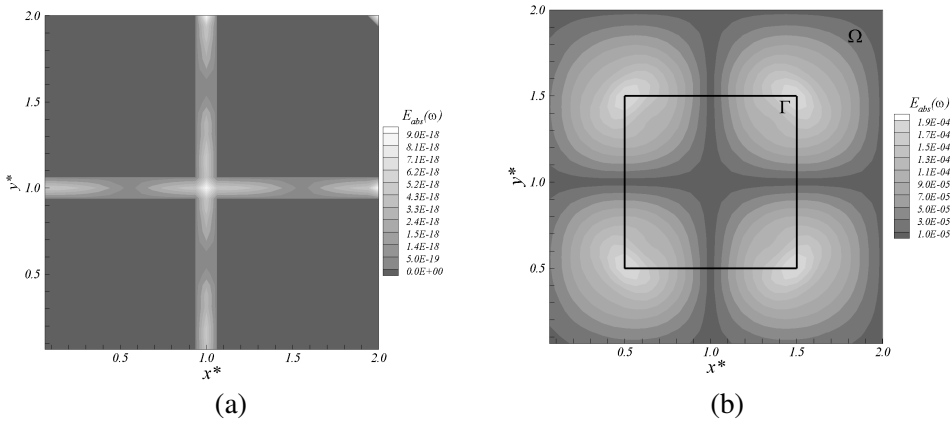

Figure 8: Absolute error of vorticity (a) whitout IB (b) with IB.

4.2   *The two-dimensional lid-driven cavity*

As explained before, the main interest of the *IMERSPEC* methodology is to simulate flows with general (non-periodic) external boundary conditions by using a classical Fourier pseudo-spectral method developed for periodic flows associated with all advantages from these methods, *i.e.* high accuracy and low computational cost. Moreover, *IMERSPEC* allows the inclusion of other boundary conditions within the flow at study, for instance resulting from the presence of complex shaped bodies.

In the present work it was decided to consider only no-slip boundary conditions. An interesting test case with which the present approach can be tested is the 2D lid-driven cavity (LDC) flow [Ghia, Ghia, and Shin (1982); Hou, Zou, Chen, Doolen, and Cogley (1995); Botella and Peyret (1998); Erturk, Corke, and Göcçöl (2005)].

This flow has been extensively studied and has been used very often in order to assess numerical codes and algorithms. It consists in a squared two-dimensional cavity of width l_x and height l_y, with $l_x = l_y = l$, where the upper wall moves from left to right with a given velocity U which drives the flow, as shown in Fig. 9. The characteristics and topology of the LDC flow depend on the Reynolds number $Re = Ul/\nu$. For $Re = 100$ the flow structure is characterized by a primary eddy

(PE) centred slightly to the upper right side of the cavity. In addition to this eddy, there are two smaller eddies at the bottom left (BLE) and at the bottom right (BRE) corners of the cavity. As the Reynolds number increases from $Re = 100$ up to $Re = 1000$, the center of the PE approaches to the center of the cavity while the size of the BLE and BRE increase. At $Re = 10000$ there is also a third eddy structure at the top left corner of the cavity. The flow solution has been shown to be stationary for Reynolds numbers of up to $Re = 10000$, and at least for $Re \approx 13000$ the flow has been shown non-stationary solutions.

The LDC flow can be simulated using the *IMERSPEC* methodology if we consider that the walls from the lid driven cavity coincide precisely with the external Lagrangian surface and delimit the interior domain Ω_I *i.e.* $\Gamma = \Gamma_{BC}$ as sketched in Fig. 9. We consider also that there are no immersed bodies in this problem. The size of the Eulerian domain $\Omega = \Omega_B \cup \Omega_I$, along the horizontal ($x$) and vertical ($y$) directions are equal to $L_x = L_y = L = 2\pi$. The ratio of Eulerian domain (Ω) in interior domain (Ω_I) sizes is represented by the parameter $\eta = L/l$ which can be varied in order to analyse the influence of the buffer domain size over the results.

4.2.1 Results for different Reynolds numbers

We start analysing the simulation of the LDC flow at different Reynolds numbers $Re = 100$, $Re = 400$ and $Re = 1000$, before exploring the effects of some parameters on the accuracy of the results. A simulation for these Reynolds numbers was carried
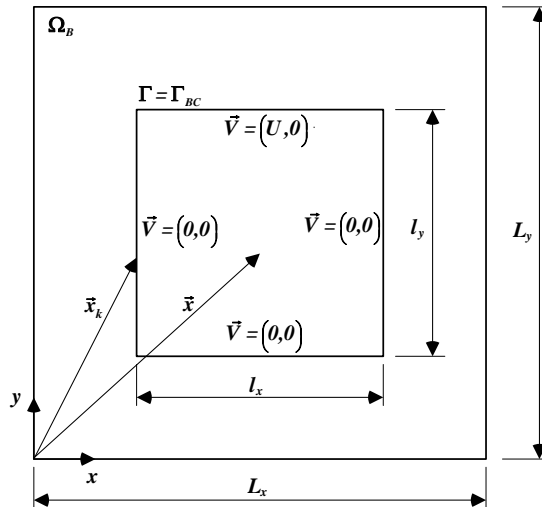

Figure 9: Sketch of domain for LDC.

out using the *IMERSPEC* methodology with $\eta = 2.0$ and using a grid with $N_x = N_y = 256$ collocation points along the x and y directions. Thus, the number of points used to describe the cavity along each direction was $N_{cav} = N_x/\eta = N_y/\eta = 128$, while the buffer domain uses $N_B \times N_B = (N_x - N_{cav}) \times (N_y - N_{cav}) = 128 \times 128$ grid points. The Courant number was $CFL = 0.01$.

A global idea of the results obtained for these simulations can be gained by looking into Fig. 10, which shows contours of the u-velocity and the streamlines for the entire Eulerian domain, including the interior domain of cavity, Ω_I, and the buffer domain Ω_B, outside the cavity. Fig. 10 (a) shows the well known pattern for this flow at $Re = 100$ [Ghia, Ghia, and Shin (1982); Hou, Zou, Chen, Doolen, and Cogley (1995)], with a large recirculating region near the center of the cavity - the primary eddy (PE) - and with two smaller (secondary) recirculation regions at each corner of the bottom wall. The biggest of these secondary bubbles lies near the bottom right wall of the cavity - bottom right eddy (BRE) - while the smaller bubble rest at the bottom left wall - bottom left eddy (BLE). In the buffer domain the streamlines show how the flow adjusts itself to the imposed conditions on Γ_{BC}. The top wall of the cavity drives the flow inside the cavity as the flow outside it. This creates a strong left-right current in the upper part of the buffer domain $(-0.5 < x^* < 1.5$ and $1.0 < y^* < 1.5)$ that dominates the flow in the upper buffer domain region.

At Fig. 10, a big recirculation region in the right side of the cavity dominates flow in the buffer domain in $1.0 < x^* < 1.5$ and $0.0 < y^* < 1.0$. This big eddy is centred at $(x^*, y^*) = (1.4, 0.7)$, due to the periodic boundary conditions imposed in the external domain, this same recirculation appears at the left side of the external domain in $-0.5 < x^* < 0.0$ and $0.0 < y^* < 1.0$ and also drives a left-right current in the lower part of the buffer domain $(-0.5 < x^* < 1.5$ and $-0.5 < y^* < 0.0)$, which is consistent with the existence of periodic boundary conditions in all the external (Eulerian) boundaries. Here, we notice the existence of a stagnation point about $x^* \approx 1.25$ and $y^* \approx 0.0$, and of a small recirculation bubble in the buffer domain near $x^* \approx 1.0$ and $y^* \approx 0.0$.

In order to analyse the influence of the Reynolds number in the present *IMERSPEC* methodology Fig. 10 (b) and (c) show contours of u-velocity and streamlines at $Re = 400$ and $Re = 1000$, respectively. These two simulations are very similar to the ones found in the literature [Ghia, Ghia, and Shin (1982); Hou, Zou, Chen, Doolen, and Cogley (1995)]. Comparing the LDC flow at $Re = 100$ and $Re = 400$, we see that the center of the PE has shifted towards the center of the cavity for higher Reynolds numbers. Furthermore, the size of the two secondary eddies at the bottom wall of the cavity has also slightly increased. Tabs. 1 and 2 show that the vorticity intensity of the PE and the coordinates of the center of the PE, BLE and
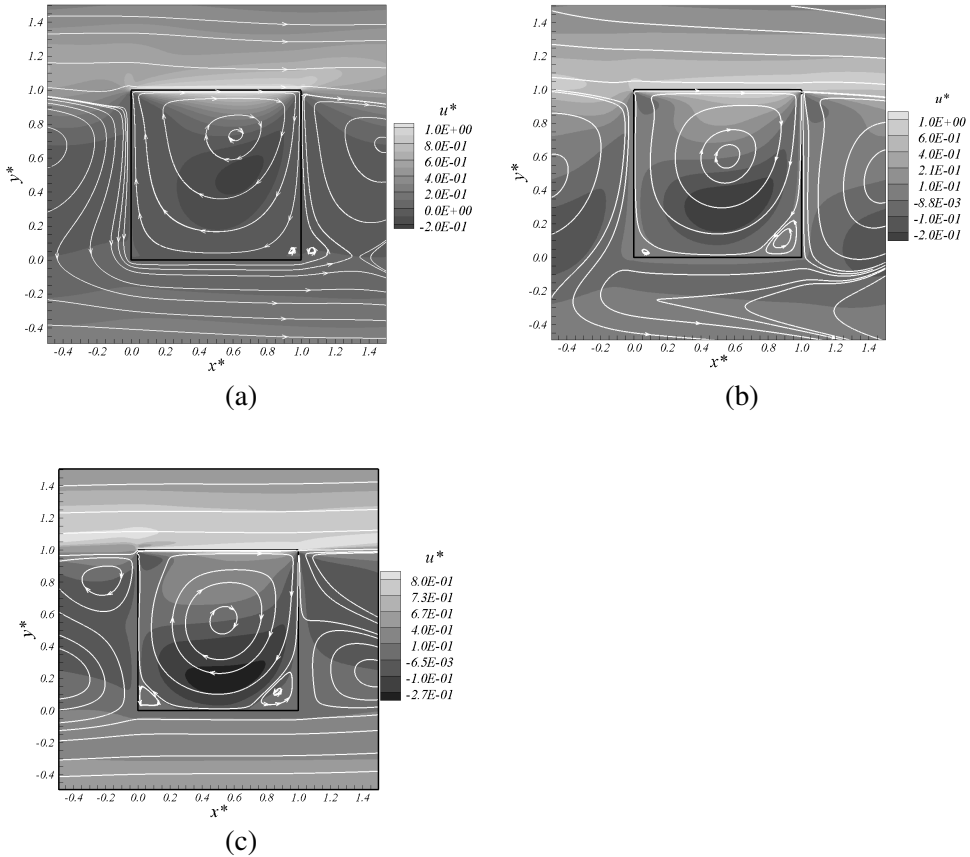
Figure 10: Simulation of LDC u-velocity field and stream-lines (a) $Re = 100$, (b) $Re = 400$ and (c) $Re = 1000$.

BRE agree well with the reference values found on the literature.

It is interesting to understand the dynamics of the flow in the buffer region by considering the effects of the source term prescribed at the immersed boundaries. Indeed the nature of the immersed boundary technique used in this work implies that at interior wall boundary we have

$$U_{wall} \approx \frac{U_{ext} + U_{int}}{2}, \tag{26}$$

where U_{wall} is the velocity at the wall, and U_{ext} and U_{int} are the velocities inside and external of the cavity (see [Silva, Silveira-Neto, and Damasceno (2003)]). This explains the behavior of the streamlines near each one of the four walls delimiting

the Γ_{BC} boundary. Indeed, near the top wall boundary which drives the flow ($0.0 < x^* < 1.0$ and $y^* = 1.0$), the streamlines at both sides *i.e.* for $y^* > 1.0$ and $y^* < 1.0$ have the same direction. On the other hand, near the other cavity walls that at each side the streamlines pattern indicates that the internal/external cavity flows are in opposite directions, which is also consistent with the no-slip boundary condition over a wall with velocity equal to zero.

The global flow pattern observed near the four walls can be explained by the moving wall at the cavity top and by the periodicity of the external boundary conditions, as well as the nature of the no-slip boundaries in the cavity walls, as described by Eq. (26).

Tab. 1 displays the vorticity intensity of the primary eddy (PE) for the present simulations compared to the results of [Ghia, Ghia, and Shin (1982); Hou, Zou, Chen, Doolen, and Cogley (1995)]. As can be seen, for $Re = 100$, $Re = 400$ and $Re = 1000$, the vorticity intensity agrees well with the values from the literature. Tab. 2 shows the coordinates of the center of the primary (PE), bottom left (BLE) and bottom right (BRE) eddies in the present work and in the simulations of [Ghia, Ghia, and Shin (1982); Hou, Zou, Chen, Doolen, and Cogley (1995)]. The present results agree very well with the values from literature, except for the location of smaller secondary BLE, for $Re = 100$, where the present results show some discrepancy. Figs. 11 (a), (b) and (c) show contours of u-velocity and pressure with the streamlines for the LDC flow. Notice that only the interior domain of the flow (Ω_I) is shown here. Compared to the same figures in [Ghia, Ghia, and Shin (1982)] and [Hou, Zou, Chen, Doolen, and Cogley (1995)] at the same Reynolds number we can see that excellent agreement is found for all these variables. Finally, in order to make a quantitative comparison of the results from the present simulation with the results from the literature, Figs. 12 (a) and (b) show mean u and v velocities profiles for the LDC flow at $Re = 100$ taken at $x^* = 0.5$ and $y^* = 0.5$ respectively.

Table 1: Vorticity intensity of the primary eddy (PE) for several Reynolds numbers $Re_h = 100$, 400 and 1000 compared to the simulations of references [Ghia, Ghia, and Shin (1982); Hou, Zou, Chen, Doolen, and Cogley (1995); Botella and Peyret (1998); Erturk, Corke, and Göcçöl (2005)].

Reference	$Re = 100$	$Re = 400$	$Re = 1000$
Ghia, Ghia, and Shin (1982)	3.17	2.29	2.05
Hou, Zou, Chen, Doolen, and Cogley (1995)	3.13	2.29	2.08
Botella and Peyret (1998)	—	—	2.07
Erturk, Corke, and Göcçöl (2005)	—	—	2.06
Present work	3.11	2.19	2.02

As can be seen, the present results display a very good agreement with the classical results by [Ghia, Ghia, and Shin (1982)], for both velocity components. we also
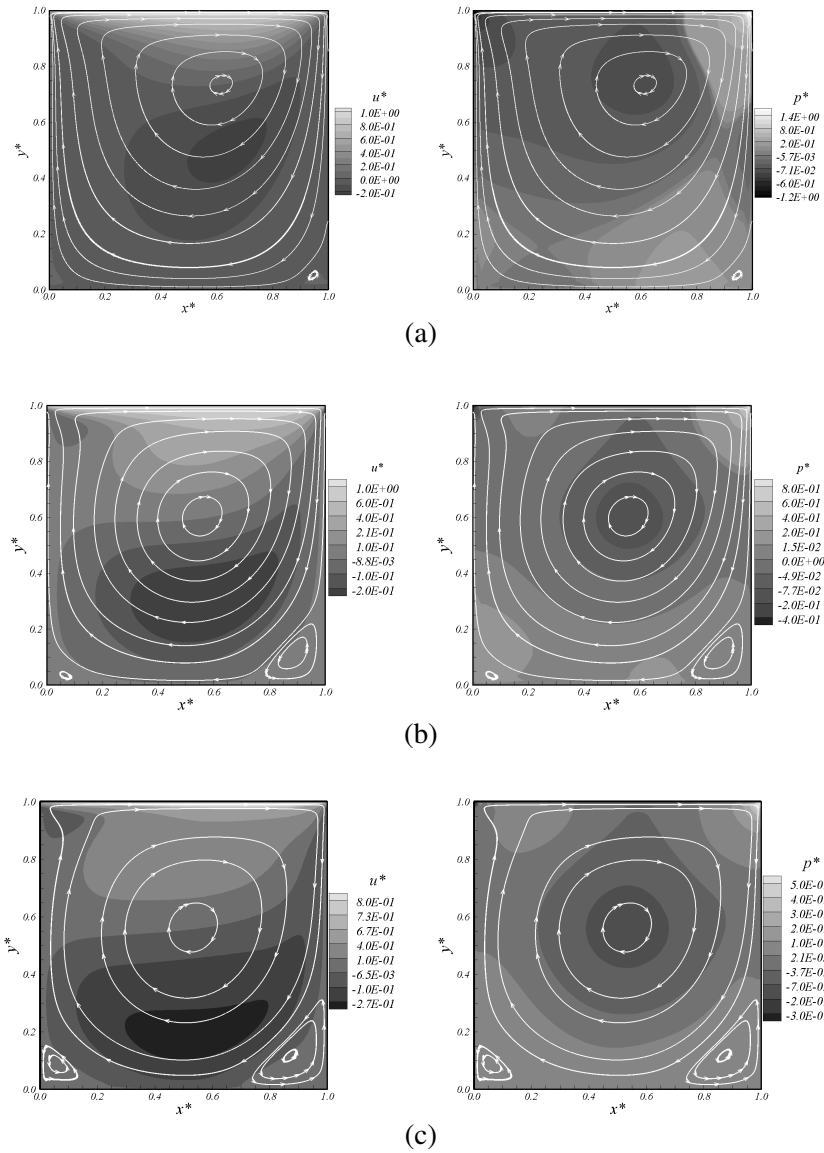

(a)

(b)

(c)

Figure 11: Simulation of LDC u-velocity in column left and pressure in column right (a) $Re = 100$, (b) $Re = 400$ and (c) $Re = 1000$.

Table 2: Coordinates of the center of the primary eddy (PE), bottom left eddy (BLE) and bottom right eddy (BRE) for several Reynolds numbers $Re_h = 100$, 400 and 1000 compared to the simulations of references [Ghia, Ghia, and Shin (1982)] and [Hou, Zou, Chen, Doolen, and Cogley (1995)].

Re	Eddy Position	[Ghia, Ghia and Shin (1982)]	[Hou, Zou,Chen Doolen and Cogley (1995)]	Present work
100	PE	(0.617;0.734)	(0.620;0.737)	(0.618;0.735)
	BLE	(0.031;0.039)	(0.039;0.035)	(0.022,0.017)
	BRE	(0.945;0.063)	(0.945;0.063)	(0.946;0.054)
400	PE	(0.555;0.606)	(0.561;0.608)	(0.558;0.603)
	BLE	(0.051;0.047)	(0.055;0.051)	(0.067;0.036)
	BRE	(0.891;0.125)	(0.890;0.126)	(0.885;0.112)
1000	PE	(0.531;0.563)	(0.533;0.565)	(0.533;0.563)
	BLE	(0.086;0.078)	(0.090;0.078)	(0.062;0.088)
	BRE	(0.859;0.109)	(0.867;0.114)	(0.870;0.116)

notice that the degree of agreement for two velocity profiles seems to be equally good for all the points in the velocity profiles.

Figures 12 (c) and (d) display *u* and *v* velocities profiles for the simulation with $Re = 400$. Although, the agreement observed is not as good as with smaller Reynolds number, the present results show an overall good agreement with the reference results from [Ghia, Ghia, and Shin (1982)]. The Figs. 12 (e) and (f) show the *u* and *v* velocities profiles for the simulation with $Re = 1000$. We see again, that the present results display a good agreement with the reference results for this flow.

The above results have shown that the *IMERSPEC* method is capable of reproducing accurately the most important features of the 2D LDC flow, which gives us confidence in the method. The present results are indeed encouraging as they clearly show the potential of the present method. Even if a more detailed analysis of the errors is desirable, for instance near the solid boundaries, L_2 norm, Eq. (25), is calculate over cavity boundaries (Γ_{BC} domain), where ϕ_a are velocities at the walls and ϕ is the solutions of simulations. Theoretically L_2 norm should be zero, however, an error over the boundaries, as shows in Fig. 13 presents order of 3.4×10^{-2}. In summary, we see that the Reynolds number has a small influence on the accuracy of the results obtained with the *IMERSPEC* methodology. In order to do further test with this methodology next sections describe the effects of the size of the buffer domain in the accuracy of the results for the LDC flow.
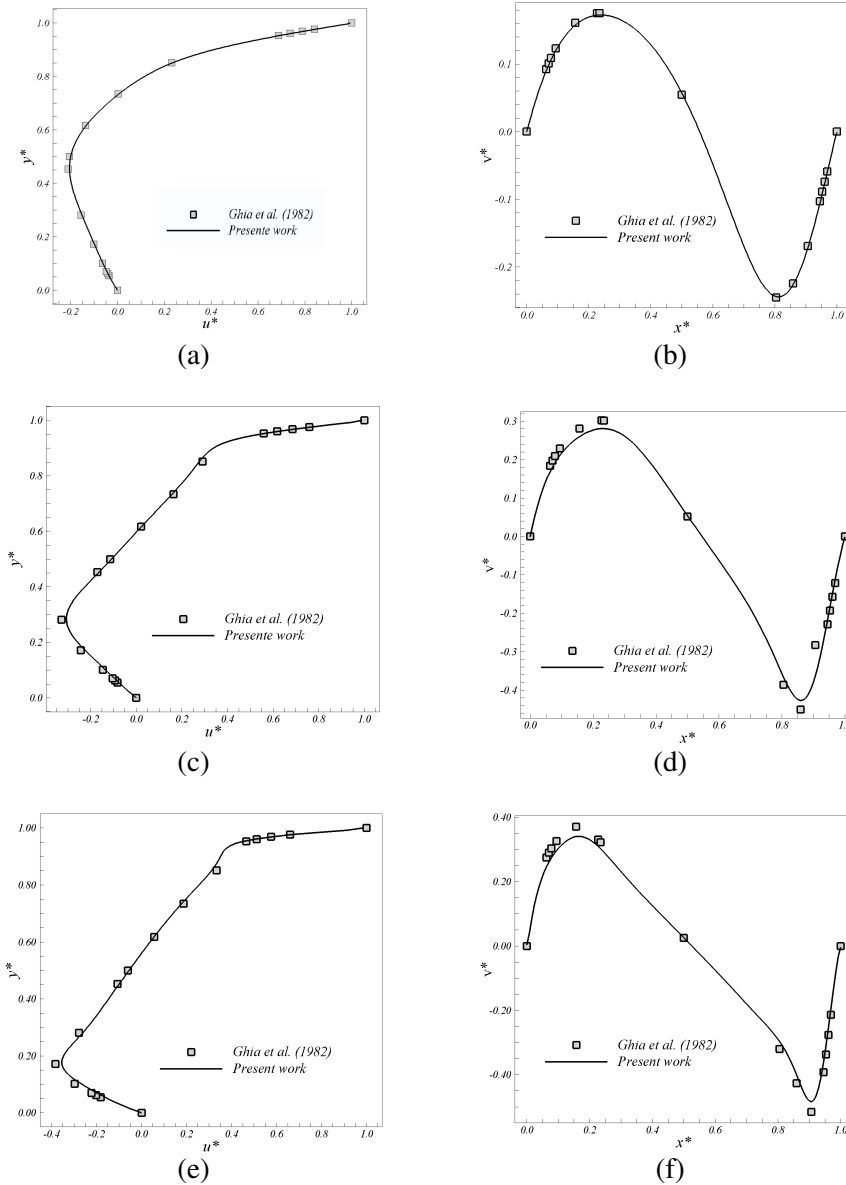
Figure 12: Profiles of LDC $Re = 100$ (a) u-velocity (b) v-velocity; $Re = 400$ (c) u-velocity (d) v-velocity and $Re = 1000$ (e) u-velocity (f) v-velocity.

4.2.2 Influence of the external domain size

Since the present *IMERSPEC* methodology uses a buffer domain to connect the flow of interest and the total computational domain, it is important to analyse the
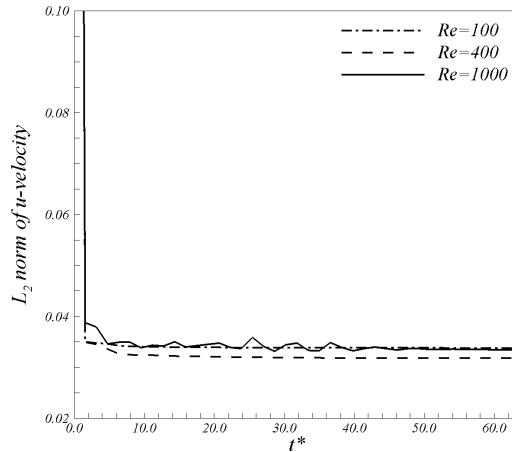
Figure 13: Temporal evolution of L_2 norm.

effect of the size of this buffer domain zone in the accuracy and characteristics of the results obtained. For this purpose additional simulations of the LDC flow for $Re = 1000$ are carried out by using more four different buffer domain sizes, $\eta = 1.17$, $\eta = 1.26$, $\eta = 1.5$ and 3.0, and by using always the same number of collocation points within cavity $N_{cav} \times N_{cav} = 64 \times 64$. Thus a different spatial resolution was used outside the cavity zone for the simulations, with $N_x \times N_y = (N_{cav} \times \eta) \times (N_{cav} \times \eta) = 75 \times 75$, 81×81, 96×96 and 192×192, for $\eta = 1.17$, $\eta = 1.26$, $\eta = 1.5$ and 3.0, respectively. Consequently the total number of points used to described the buffer domain was equal to $N_B \times N_B = (N_x - N_{cav}) \times (N_y - N_{cav}) = 11 \times 11$, 17×17, 32×32 and 128×128. The reference simulation with $\eta = 2.0$ used $(N_x \times \eta) \times (N_y \times \eta) = 128 \times 128$ and $N_B \times N_B = (N_x - N_{cav}) \times (N_y - N_{cav}) = 64 \times 64$ grid points, for the cavity and buffer domains, respectively. Fig. 14 displays the entire computational domain and the interest domain for the simulations showing streamlines and vorticity contours. The figures 14 (a)-(f) show that the streamlines pattern in the buffer domain is very different for three simulations, as expected. In particular, the size, the number and the location of the large recirculation regions in the buffer region Ω_B changes with η. Notice, however, that the periodicity of the external boundaries is maintained in all three situations.

For $\eta = 1.17$ has only $N_x \times N_y = 75 \times 75$ collocation points, however it is possible to see periodicity influence in the secondary recirculation inside the cavity. For $\eta = 1.26$, $\eta = 1.5$ and $\eta = 2.0$ no differences are observed. For $\eta = 3.0$ a secondary recirculation arises at the left top conner. In the other hand, Fig. 15 shows the temporal evolution of L_2 norm at cavity boundaries conditions. For $\eta = 2.0$ and
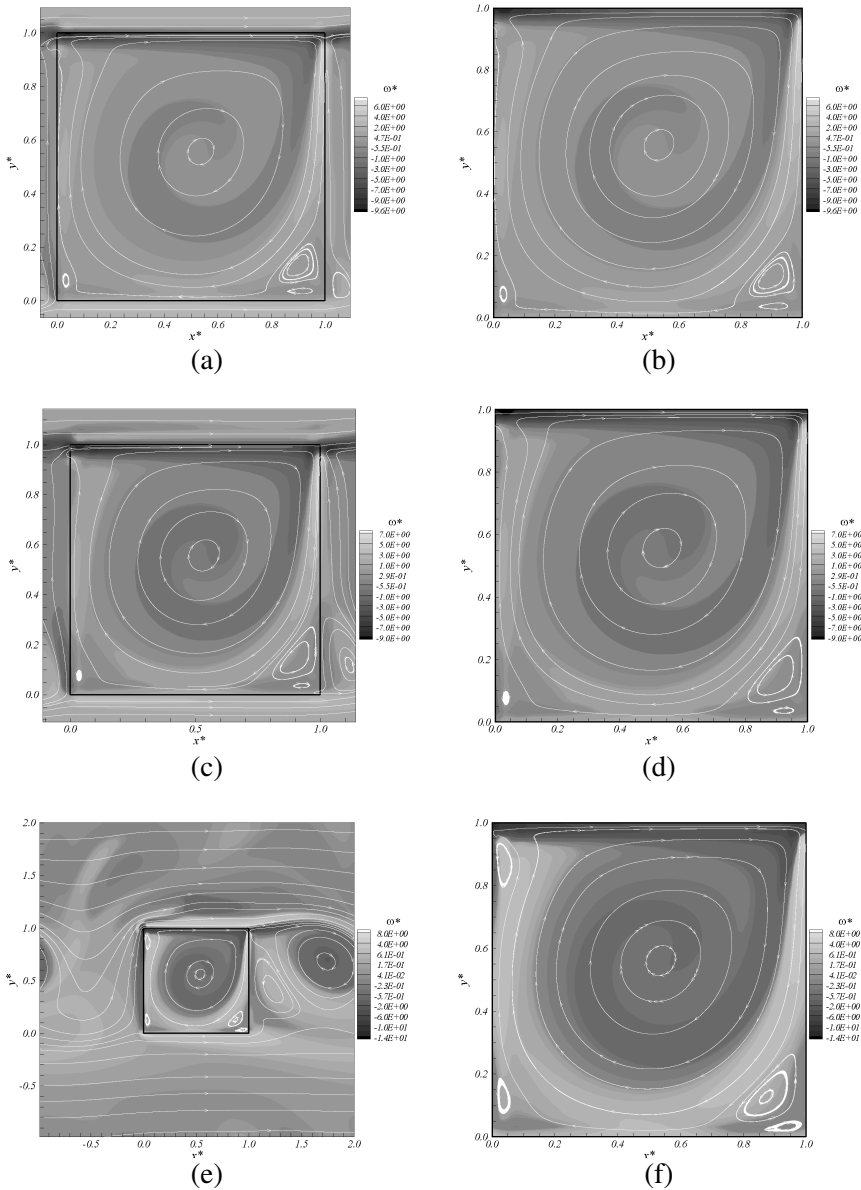
Figure 14: Vorticity field of LDC $Re = 1000$ for (a) whole domain $\eta = 1.17$, (b) interest domain $\eta = 1.17$, (c) whole domain $\eta = 1.26$, (d) interest domain $\eta = 1.26$, (e) whole domain $\eta = 3.0$ and (f) interest domain $\eta = 3.0$.

$\eta = 3.0$ there are strong oscillations in time. As η decreases these oscillations disappear and the results become smooth and roughly independent of η parameter.

Comparing the flow topology for the five simulations and the temporal evolutions of L_2 norm we have a compromise between external and internal domain. If, the η is too small, the external boundary conditions (periodicity) influences the interior of LDC. When η is too big, flow of external domain becomes instable and also influences the internal domain. In the present analysis, $\eta = 1.26$ is the most viable.

It is well known that an exact prescription of the wall boundary conditions cannot be achieved with any immersed boundary method (*e.g.* see [Peskin (1972); Choi, Oberoi, Edwards, and Rosati (2007); Silva, Silveira-Neto, and Damasceno (2003)], since the majority of the immersed boundary methods, currently in use, consist of adding a forcing function to the Navier-Stokes equations to impose an approximate boundary conditions at the walls. Thus, it is well known that a non-zero (though small) error is always involved in these methods. In the case of the LDC, the L_2 norm for the velocity at the boundaries presents high values ($\sim 10^{-2}$) due to the discontinuities over the corners at the upper wall. At these corners the u-velocity changes from zero (over the side walls) to $u \neq 0$ (over the upper wall).

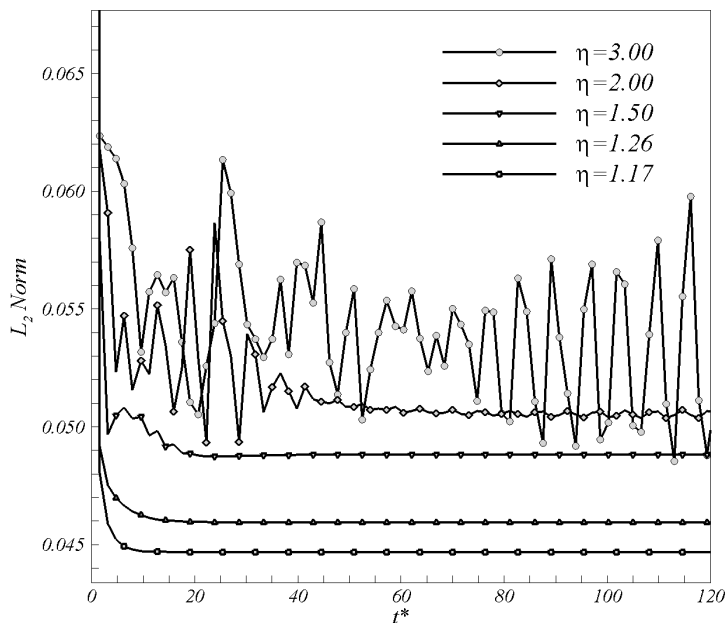The fact that different values of η lead to differences in the flow solution means

Figure 15: Temporal evolution of L_2 norm at $Re = 1000$ for different η ratios.

that more work may be needed in order to improve the near wall treatment of the *IMERSPEC* method. However, the results from this first test are indeed encouraging.

4.2.3 Influence of the grid size

In this section the influence of grid size is analyzed by using $\eta = 1.26$ and CFL=0.1 simulations at Re=1000 are performed changing the grid size, *i.e.* $N_{cav} \times N_{cav} = 64 \times 64$, $N_{cav} \times N_{cav} = 128 \times 128$ and $N_{cav} \times N_{cav} = 256 \times 256$.

The Fig. 16 shows the horizontal $u*$ and vertical $v*$ velocities profiles. These figures show that the results become independent of the grid as the refinement is increased. Fig. 17 presents the L_2 norm (Eq. (25)) of velocity on the walls of

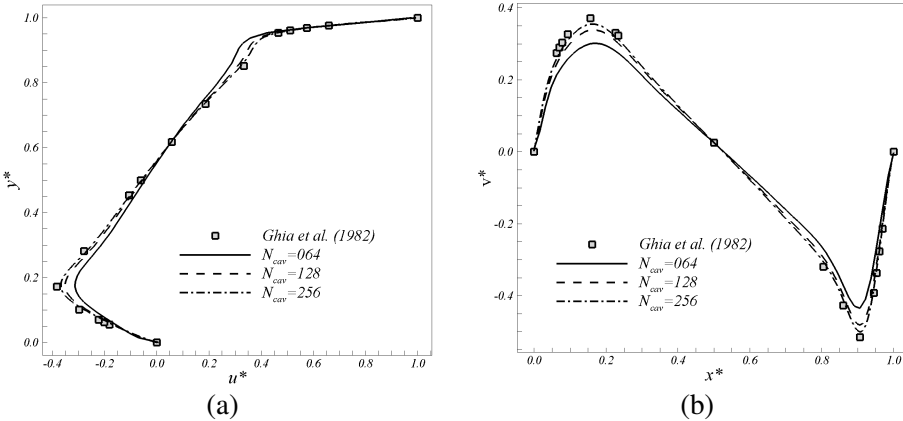

Figure 16: Profiles of LDC $Re = 1000$ (a) u-velocity (b) v-velocity.

cavity. With this result it is possible to estimate the convergence rate of method. [Ferziger and Peric (1996)] show in his book the equation for calculate the order convergence rate:

$$q = \frac{log\left(\frac{\phi_{2h} - \phi_{exact}}{\phi_h - \phi_{exact}}\right)}{log2}, \tag{27}$$

where q is the convergence rate; ϕ is the variable analyzed (in the present case, ϕ is the velocity). L_2 is the norm of the velocity at the cavity walls; h is the grid size and ϕ_{exact} is the exact solution of interest variable, *i.e.* $\phi_{exact} = 0$, over the botton and side walls, and $\phi_{exact} = U_{lid}$, over the upper wall.
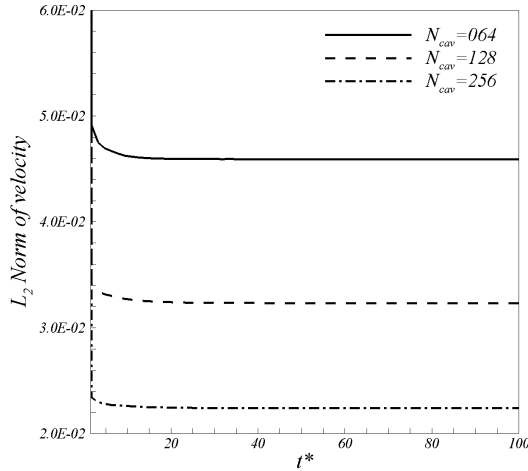
Figure 17: Temporal evolution of L_2 norm of boundary u-velocity over the boundary Γ.

According to Fig. 17 the convergence rate of these simulations is, approximately, $q = 1.45$. The low order is due to the singularity points on the conners of the cavity at the superior conners, as explained by [Botella and Peyret (1998)].

4.3   *Flow over a square cylinder*

Results for the flow over a square cylinder are shown as another example of a non-periodic flow that can be handled using the *IMERSPEC* methodology *i.e.* the Navier-Stokes equations are solved using the Fourier pseudo-spectral method, and the boundary conditions have been imposed through a force field of the immersed boundary. The simulations consist of an inlet uniform profile with velocity U_∞ [m/s], which flows over a square cylinder (Fig. 18).

Quantities such as drag (Eq. (28)) and lift coefficients (Eq. (29)) are analyzed. These parameters depend on the force acting on the bodies immersed in the flow. The drag coefficient determines the resistance force on the fluid caused by the immersed body, while the lift coefficient determines the force that acts on the normal direction of the incoming flow:

$$Cd = \frac{2F_x}{\rho A_x U_\infty^2}, \tag{28}$$

$$Cl = \frac{2F_y}{\rho A_y U_\infty^2}, \tag{29}$$

where A_x and A_y are the projected frontal area in perpendicular direction x and y, respectively, given in $[m^2]$. F_x and F_y are the force components in each direction and are given by:

$$F_x = \sum_{k=1}^{N_l} \vec{F}(\vec{x}_k).\vec{n}_x, \tag{30}$$

$$F_y = \sum_{k=1}^{N_l} \vec{F}(\vec{x}_k).\vec{n}_y, \tag{31}$$

where $\vec{F}(\vec{x}_k)$ is given by Eq. (14) and $\vec{n}_x$ and $\vec{n}_y$ are:

$$\vec{n}_x = \frac{(x_k,0)}{||(x_k,0)||}, \tag{32}$$

$$\vec{n}_y = \frac{(0,y_k)}{||(0,y_k)||}. \tag{33}$$

Another important parameter is the Strouhal number, Eq. (34), which represents the non-dimensional frequency of vortex shedding. The Strouhal number is given by:

$$St = \frac{f_r D}{U_\infty}, \tag{34}$$

where f_r is the frequency $[1/s]$ of vortex shedding downstream of the cylinder, wich is obtained from the analysis of the frequency spectrum of lift coefficient, and D is diameter of the cylinder. The domain simulated is equal to $64D \times 32D$, where
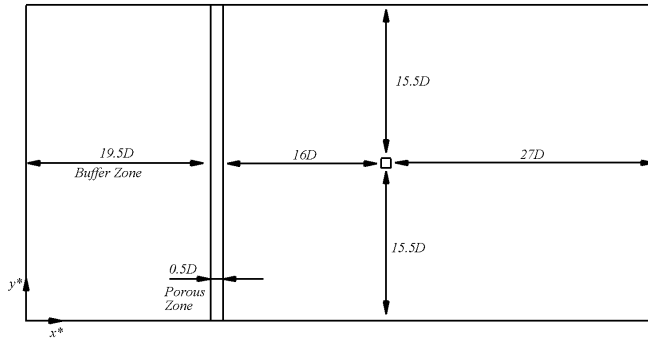

Figure 18: Sketch of domain for flow over square cylinder.

$D = \pi/16\,[m]$, and it is discretized with 1024×512 collocation points. The cylinder
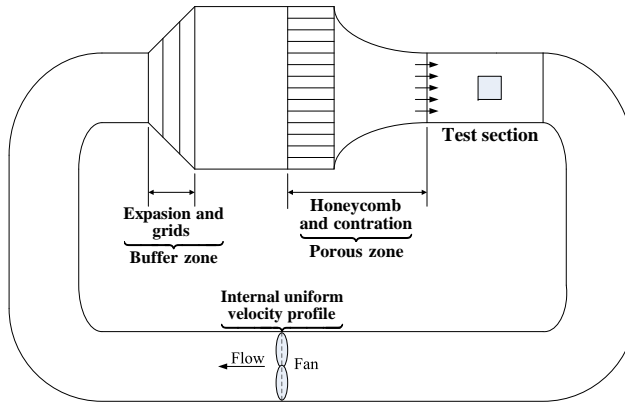
Figure 19: Sketch of wind tunnel of closed-circuit.

has 64 lagrangean points, (16 for each face) and the cylinder center position in domain is $x^* = 36.5D$ and $y^* = 15.5D$, where $x^* = x/D$ and $y^* = y/D$. The sketch of the domain is shown in Fig. 18.

Periodic boundary conditions have been imposed, but a uniform profile of velocity $(U_\infty = 1.0 \ [m/s])$ is set through the force field of the immersed boundary method, at $x^* = 20D$.

The vortex street caused by the cylinder is transported toward the domain outlet, and it is injected at the domain inlet by the periodic boundary condition. A buffer zone (BZ) is used in order to damp these vortices and to prevent disturbing the internal velocity profile imposed inside the domain (upstream of the cylinder), through the immersed boundary method. This *BZ* is similar to one use by [Uzun (2003)]:

$$BZ = \phi \left(Q_i - Qt_i \right), \tag{35}$$

where Q_i is the solution of problem, *i.e.*, u and v. Qt_i is the target solution, which represents the solution required in the final buffer zone. The target solution is, for example, the uniform profile U_∞ and ϕ is the parameter of damping vortex calculated by Eq. (36):

$$\phi_\eta = \beta \left(\frac{x_\eta - x_{BZ}}{x_f - x_{BZ}} \right)^\alpha, \tag{36}$$

where $\alpha = 3.0$ and $\beta = 1.0$, x_{BZ} and x_f are the beginning and the ending of *BZ*, respectively, and x_η is the generic position. Notice that the location of the *BZ* *i.e.* if it is placed downstream or upstream of the cylinder, it does not modify

the results. In addition to the *BZ* a porous zone (*PZ*) is also imposed after the *BZ* consisting in a uniform velocity field. The authors have tried to simulate a
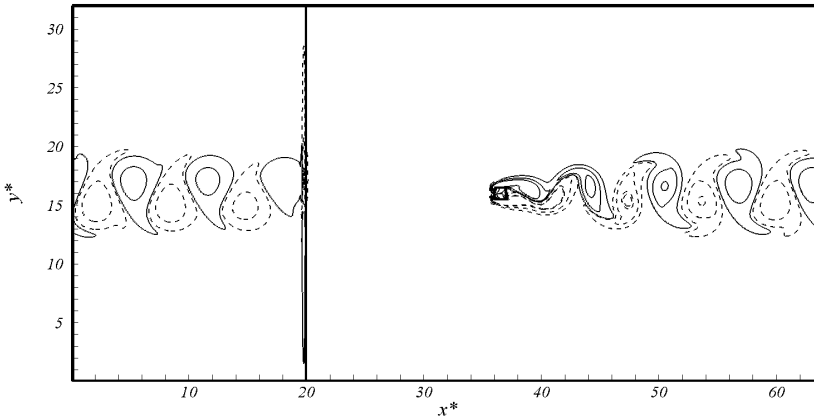

Figure 20: Flow over square cylinder at Re=100, vorticity field, $\omega = -1.0$, solid line, and $\omega = 1.0$, dashed line.

wind tunnel that works in closed circuit, Fig. 19 illustrate this idea. The system fan is simulated by the velocity profile imposed inside the domain by immersed boundary method. The vortex damping system of the wind tunnel (expansions, grids, contraction and honeycomb) is modeled using the buffer zone and the porous zone. The closed circuit is modeled by periodic boundary conditions. We carried
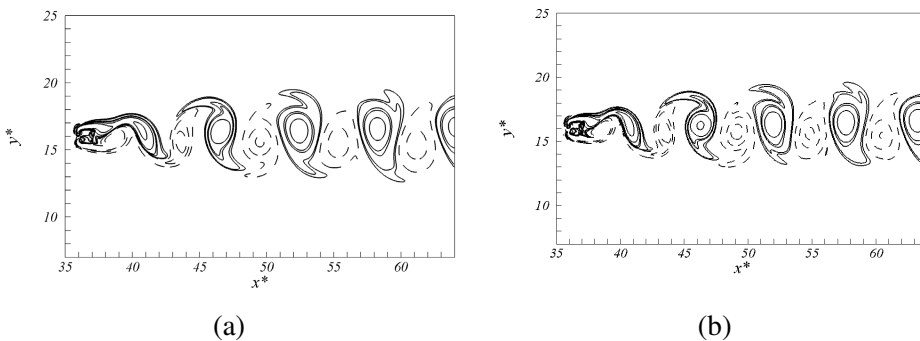

(a)   (b)

Figure 21: Flow over square cylinder, vorticity field, $\omega = -1.0$, solid line, and $\omega = 1.0$, dashed line. (a) Re=150, (b) Re=200.

out three simulations with different Reynolds number (100, 150 and 200) based on

the cylinder side (D) and using $CFL = 0.1$. Fig. 20 shows the vorticity field for the flow at Re=100 at t*= 500. The figure displays the vortex shedding, the inlet velocity profile position and buffer zone influence. Fig. 21 shows the vorticity field for Re=150 and Re=200. The karman vortex street is very well captured. Moreover, the vortices are well aligned with the x-direction as expected in two dimensional simulations. The non-periodic boundary conditions are well represented by the proposed methodology.

The Tab. 3, shows a comparison with other authors. For instance [Silva, Silveira-Neto, and Damasceno (2003)] has used the same immersed boundary method used in the present work (Virtual Physical Model), but discretized by second order finite differences. The results from [Fuka and Brechler (2007)] are also shown. In this case a variant of the immersed boundary method with direct forcing method was used. The results are very similar which, again, validates the present *IMERSPEC* methodology.

Table 3: Comparison of drag coefficient and Strouhal number.

Authors	Re	$\overline{Cd}$	*St*
Silva, Silveira-Neto, and Damasceno (2003)	100	1.730	0.140
Fuka and Brechler (2007)	100	1.620	0.140
Present work	100	1.644	0.145
Silva, Silveira-Neto, and Damasceno (2003)	150	1.720	0.150
Fuka and Brechler (2007)	150	1.630	0.150
Present work	150	1.676	0.156
Silva, Silveira-Neto, and Damasceno (2003)	200	1.730	0.160
Fuka and Brechler (2007)	200	1.650	0.145
Present work	200	1.748	0.165

5   Conclusions

In the present paper a new methodology for mathematical modeling of non periodic flows, using Fourier pseudo-spectral method coupled with immersed boundary method - *IMERSPEC* - has been proposed. This methodology use the advantages of Fourier pseudo-spectral methods with the ability to handle non-periodic domains and bodies with arbitrary shape. The main idea consists in the definition of a buffer domain where any boundary condition can be imposed through the immersed boundary methods. In addition, any given immersed body can be also included in the computational domain. The method is applied to the lid-driven cavity flow, and to the flow over a rectangular cylinder. We have been obtained good

results in our study.

References

Barton, I.; Markham-Smith, D.; Bressloff, N. (2002): Finite volume scheme for the solution of fluid flow problems on unstructured non-staggered grids. *Int. J. Numer. Methods Fluids*, vol. 38(8), pp. 747–768.

Berland, J.; Bogey, C.; Bailly, C. (2006): Low-dissipation and low-dispersion fourth-order runge-kutta algorthim. *Computers and Fluids*, vol. 35, pp. 1459–1463.

Botella, O.; Peyret, R. (1998): Benchmark spectral results on the lid-driven cavity flow. *Computer and Fluids*, vol. 27(4), pp. 421–433.

Briggs, W.; Henson, V. (1995): *The DFT*. SIAM.

Canuto, C.; Hussaini, M. Y.; Quarteroni, A.; Zang, T. A. (1987): *Spectral Methods in Fluid Dynamics*. Springer-Verlag.

Chen, C.; Chang, S.; Sun, S. (2007): Lattice boltzmann method simulation of channel flow with square pillars inside by the field synergy principle. *CMES: Computer Modeling in Engineering Sciences*, vol. 22, pp. 203–215.

Choi, J.; Oberoi, C.; Edwards, J. C.; Rosati, J. A. (2007): An immersed boundary method for complex incompressible flows. *J. Comp. Phys.*, vol. 224, pp. 757–784.

Cooley, T.; Tukey, J. (1965): An algorithm for the machine calculation of complex fourier series. *Mathematics Computation*, vol. 19, pp. 297–301.

da Silva, C.; Pereira, J. (2004): The effect of subgrid-scale models on the vortices obtained from large-eddy simulations. *Phys. Fluids*, vol. 16(12), pp. 4506–4543.

da Silva, C.; Pereira, J. (2005): On the local equilibrium of the subgrid-scales: The velocity and scalar fields. *Phys. Fluids*, vol. 17, pp. 108103.

Erturk, E.; Corke, T.; Göççöl, C. (2005): Numerical solutions of 2-d steady incompressible driven cavity flow at high reynolds numbers. *Int. J. Numer. Methods Fluids*, vol. 48, pp. 747–774.

Ferziger, J. H.; Peric, M. (1996): *Computational Methods for Fluid Dynamics*. Springer.

Fuka, V.; Brechler, J. (2007):   High resolution flow modelling for meteorological purposes. *WDS'07 Proceedings of Contributed Papers*, vol. 3, pp. 150–155.

Ghia, U.; Ghia, K. N.; Shin, C. T. (1982):   High-re solutions for incompressible flow using the navier-stokes equations and a multigrid method.   *J. Comp. Phys.*, vol. 48, pp. 387–411.

Goldstein, D.; Adachi, T.; Sakata, H. (1993):   Modeling a no-slip flow with an external force field. *J. Comp. Phys.*, vol. 105, pp. 354.

Hou, S.; Zou, Q.; Chen, S.; Doolen, G.; Cogley, A. (1995):   Simulation of cavity flow by the latice boltzmann method. *J. Comp. Phys.*, vol. 118, pp. 329–347.

Iaccarino, G.; Verzicco, R. (2003):   Immersed boundary technique for turbulent flow simulations. *Appl. Mech. Rev.*, vol. 56(3), pp. 331–347.

Johansen, H.; Collela, P. (1998):   A cartesian grid embeded boundary method for poisson's equation on irregular domains. *J. Comp. Phys.*, vol. 147, pp. 60–85.

Kalitzin, G.; Iccarino, G. (2003):   Towards an immersed boundary solver for rans simulations. *AIAA Pap.*, pg. 0770.

Karniadakis, G.; Sherwin, S. (1999):   *spectral/hp element methods for CFD*. Oxford University Press, Oxford.

Kim, J.; Kim, D.; Choi, H. (2001):   An immersed-boundary finite-volume method for simulation of flow in complex geometries. *J. Comp. Phys.*, vol. 171, pp. 132–150.

Kobayashi, M.; Pereira, J.; Pereira, J. (1999):   A conservative finite-volume second order accurate projection method on hybrid unstructured grids. *J. Comp. Phys.*, vol. 150(1), pp. 40–75.

Kopriva, D. (1986):   A spectral multidomain method for the solution of hyperbolic systems. *Applied Numerical Mathematics*, vol. 2, pp. 221–241.

Lai, M.-C.; Peskin, C. S. (2000):   An immersed boundary method with formal second-order accuracy and reduced numerical viscosity. *J. Comp. Phys.*, vol. 160, pp. 705–719.

Lele, S. (1992):   Compact finite difference schemes with spectral-like resolution. *J. Comp. Phys.*, vol. 103, pp. 15–42.

Marchioli, C.; Armenio, V.; Soldati, A. (2007):   Simple and accurate scheme for fluid velocity interpolation for eulerian lagrangian computation of dispersed flows in 3d curvilinear grids perturbations. *Computer and Fluids*, vol. 36(7), pp. 1187–1198.

Mariano, F. (2007): Simulação de escoamentos não-periódicos utilizando as metodologias pseudo-espectral e da fronteira imersa acopladas. *Universidade Federal de Uberlandia*, vol. 1, pp. 1–121.

Mavriplis, D. (1997): Unstructured grid techniques. *Annu. Rev. Fluid Mech.*, vol. 29, pp. 473–514.

Miksad, R.; Akylas, T.; Hebert, T. (1987): Non-linear interections in fluids. *ASME*, vol. 1, pp. 131–145.

Mittal, R.; Iaccarino, G. (2005): Immersed boundary methods. *Annu. Rev. Fluid Mech.*, vol. 37, pp. 239–261.

Peskin, C. S. (1972): Flow patterns around heart valves: a numerical method. *J. Comp. Phys.*, vol. 10, pp. 252–271.

Peskin, C. S. (1977): Numerical analysis of blood flow in the heart. *J. Comp. Phys.*, vol. 25, pp. 220.

Peskin, C. S. (2002): The immersed boundary method. *Acta Numerica*, vol. 11, pp. 479–517.

Silva, A. L. L. E.; Silveira-Neto, A.; Damasceno, J. J. R. (2003): Numerical simulation of the two-dimensional flows over a circular cylinder using the immersed boundary method. *J. Comp. Phys.*, vol. 189, pp. 351–370.

Silvestrini, J.; Lamballais, E. (2002): Direct numerical simulations of wakes with virtual cylinders. *Int. J. Heat and Fluid Flow*, vol. 16(4), pp. 305–314.

Sohankar, A. (2006): Flow over a bluff body from moderate to high reynolds numbers using large eddy simulation. *Computers and Fluids*, vol. 35, pp. 1154–1168.

Sousa, J. (2005): Numerical simulation of unstable flow through a spherical bulge in a 90-degree asymmetrical bend. *Computer Modeling in Engineering Sciences*, vol. 9, pp. 211–219.

Takahashi, D. (2001): A blocking algoritm for fft on cache-based processors. *Proc. 9th International Conference on High Performance Computing and Network Europe*, vol. 2110, pp. 551–554.

Taylor, G. I.; Green, A. E. (1937): Mechanism of the production of small eddies from large ones. *Phil. Trans. Roy. Soc.*, vol. 158, pp. 499–521.

Uhlmann, M. (2005): An immersed boundary method with direct forcing for the simulation of particulate flows. *J. Comp. Phys.*, vol. 209, pp. 448–476.

Unverdi, S.; Tryggvason, G. (1992): A front-tracking method for viscous, incompressible, front-tracking method for viscous, incompressible, multifluid flows. *J. Comp. Phys.*, vol. 100, pp. 25–37.

Uzun, A. (2003): 3d large-eddy simulation for jet aeroacoustics. *Purdue University - Thesis Doctorate*, vol. 1, pp. 1–213.

Xu, H.; Zhang, C. (1999): Study of the effect of the non-orthogonality for non-staggered grids - the results. *Int. J. Numer. Methods Fluids*, vol. 29(6), pp. 625–644.